



# Coexisting Attractors in a Physically Extended Lorenz System

Sungju Moon, Jong-Jin Baik\* and Seong-Ho Hong

*School of Earth and Environmental Sciences,*

*Seoul National University,*

*Seoul 08826, Republic of Korea*

*\*jjbaik@snu.ac.kr*

Received October 5, 2020

Coexisting attractors may arise from many different sources such as hidden basins of attraction or peculiarly organized bifurcation structures. By exploiting the regions of mismatched bifurcations between the system and its fixed points, this study investigates coexisting attractors in a six-dimensional extension of the Lorenz system. This six-dimensional extension takes into account additional physical ingredients, namely, rotation and density-affecting scalar, which are not considered in the original Lorenz system. These newly considered physical ingredients can influence the bifurcation structures and thus the system's characteristics with regard to coexisting attractors. Once the potential regions of coexisting attractors are identified in the parameter spaces, the coexistence of periodic and point attractors and that of two different periodic orbits in addition to the well-known coexistence of chaos and stability are demonstrated through the solution trajectories and attractor basin boundaries.

**Keywords:** Lorenz–Stenflo system; higher-dimensional Lorenz system; coexisting attractors; basin of attraction; Hopf bifurcation.

## 1. Introduction

The three-dimensional Lorenz system [Lorenz, 1963], celebrated for its seminal role in the modern development of chaos theory, can be derived from the governing equations for Rayleigh–Bénard convection. Recently, the following six-dimensional extension of the Lorenz system has been derived by considering in the governing equations two additional physical ingredients, rotation and density-affecting scalar [Moon *et al.*, 2019]:

$$\dot{X} = \sigma(Y - X) - \sigma \text{Le}^{-1}W + sV, \quad (1)$$

$$\dot{Y} = -XZ + r_T X - Y, \quad (2)$$

$$\dot{Z} = XY - bZ, \quad (3)$$

$$\dot{V} = -X - \sigma V, \quad (4)$$

$$\dot{W} = -XU + r_C X - \text{Le}^{-1}W, \quad (5)$$

$$\dot{U} = XW - \text{Le}^{-1}bU, \quad (6)$$

where  $X$ ,  $Y$ ,  $Z$ ,  $V$ ,  $W$ ,  $U$  are the variables with the dots above indicating their first derivatives with respect to time  $\tau$ . The six parameters include three familiar parameters from the original Lorenz system:  $r_T$ , the Rayleigh parameter,  $\sigma$ , the Prandtl number, and  $b$ , a geometric parameter. The three additional parameters are  $r_C$ , another Rayleigh-type parameter defined with the vertical

\*Author for correspondence

This is an Open Access article published by World Scientific Publishing Company. It is distributed under the terms of the Creative Commons Attribution-NonCommercial 4.0 (CC BY-NC) License which permits use, distribution and reproduction in any medium, provided that the original work is properly cited and is used for non-commercial purposes.

gradient of scalar concentration in place of the vertical gradient of temperature,  $Le$ , the Lewis number, and  $s$ , a rotational parameter. A detailed derivation of this six-dimensional system along with the precise definitions of these additional parameters is found in [Moon *et al.*, 2019].

A four-dimensional subset of the six-dimensional system (1)–(6), whereby only the effects of rotation are considered, is known as the Lorenz–Stenflo system. First derived in the context of acoustic-gravity waves in the atmosphere [Stenflo, 1996], the Lorenz–Stenflo system has since been intensely investigated not only for its interesting dynamical properties [Yu, 1999; Van Gorder, 2013; Park *et al.*, 2015] but also for its importance to atmospheric science [Roy *et al.*, 2019], plasma science [Stenflo & Shukla, 2009], and various other physical, biological, and engineering applications [Pal *et al.*, 2014]. Some recent studies focus on extensions or modifications of the Lorenz–Stenflo system and the ramifications of such changes [Huang *et al.*, 2014; Park *et al.*, 2016; Roy *et al.*, 2019]. The six-dimensional physically extended Lorenz system of Moon *et al.* [2019] can also be considered as one such extension. From this perspective, when studying important features of the six-dimensional system like the coexistence of multiple attractors, it can be beneficial to examine alongside and make comparisons with the Lorenz–Stenflo system.

Coexisting attractors in dissipative systems arise from the simultaneous presence of different types of solutions in the phase space so that depending on which attractor basin the initial condition belongs, there appear solutions of different types despite having the same parameter values. Three solution types are recognized in this study: chaotic, periodic, and stable. Stable solutions lead to point attractors. In contrast, periodic and chaotic attractors arise from solutions that are considered to be *nonstable*. The bifurcation structure of the Lorenz system in the  $r_T$ – $\sigma$  space reveals a brief mismatch between the Hopf bifurcation of the nontrivial fixed points and the heteroclinic bifurcation of the system toward chaos [Doedel *et al.*, 2006], leading to the coexistence of chaotic and point attractors. This kind of coexistence in the Lorenz system is interesting because it is relatively rare in the sense that it only occurs for a narrow strip of the  $r_T$ – $\sigma$  parameter space. For example, in the three-dimensional Lorenz system with the standard parameter values

$\sigma = 10$  and  $b = 8/3$ , it has been reported that  $r_T$  values between  $\sim 24.06$  and  $\sim 24.74$  result in the coexistence of chaotic and point attractors [Yorke & Yorke, 1979]. Some also argue that conceptual interpretations of such coexisting attractors may challenge the traditional view of weather as a purely chaotic system [Reyes & Shen, 2019; Shen, 2019].

Coexisting attractors in the Lorenz system have been thoroughly studied [Yorke & Yorke, 1979; Sparrow, 1982] including the possibility of coexisting hidden attractors [Munmuangsaen & Srisuchinwong, 2018], coexisting attractors in certain previously unexplored parameter ranges [Li & Sprott, 2014; Sprott, 2015], and the role of noise in inducing the transitions between different coexistence regimes [Argyris & Andreadis, 2000; Bashkirtseva & Ryashko, 2009]. There are a few studies on the bifurcation structure of the Lorenz–Stenflo system in parameter spaces using Lyapunov exponents [Xavier & Rech, 2010; Sahoo, 2013] and periodicity diagrams [Park *et al.*, 2015], and Pal *et al.* [2014] explored multistability in coupled Lorenz–Stenflo systems; however, a detailed analysis of different kinds of coexistence exhibited by the original four-dimensional Lorenz–Stenflo system based on its bifurcation structures in parameter spaces has yet to be done. While the derivation and bifurcation analysis of the six-dimensional physically extended Lorenz system in the context of the roles played by the physically-relevant parameters were given in [Moon *et al.*, 2019], coexisting attractors arising from such circumstances involving the mismatched bifurcation structures have yet to be explored in detail, which we intend to do in this study.

This study aims to systematically investigate coexisting attractors in the physically extended six-dimensional Lorenz system of Moon *et al.* [2019] under various parameter choices including those equivalent to the four-dimensional Lorenz–Stenflo system. Owing to the added complexity from having additional parameters and fixed points, the physically extended six-dimensional Lorenz system is anticipated to feature an even more elaborate bifurcation structure, providing rich grounds for multiple scenarios potentially leading to the coexistence of various different types of attractors.

## 2. Methodology

In this section, we describe the methods for detecting heteroclinic and Hopf bifurcations in the parameter spaces of the six-dimensional system. Since our

focus is on the emergence of coexisting attractors resulting from the interactions between different kinds of bifurcations, it is useful to know where in the parameter spaces these bifurcations occur and how they are affected by the extension of the Lorenz system.

Hopf bifurcation is a local bifurcation relevant to specific fixed points in our system. In addition to the trivial fixed point  $\mathbf{X}_0 = (0, 0, 0, 0, 0, 0)$ , the system has four other nontrivial fixed points  $\mathbf{X}_0^{\pm, \mp} = (X_0^{\pm, \mp}, Y_0^{\pm, \mp}, Z_0^{\pm, \mp}, V_0^{\pm, \mp}, W_0^{\pm, \mp}, U_0^{\pm, \mp})$ , where  $X_0^{\pm, \mp}$  are given by

$$X_0^{\pm, \mp} = \pm \sqrt{\frac{-B \mp \sqrt{B^2 - 4AC}}{2A}} \quad (7)$$

with

$$A = \frac{\sigma^2 + s}{\sigma \text{Le}^{-2} b^2}, \quad (8)$$

$$B = \frac{\sigma r_C}{b} - \frac{\sigma r_T}{\text{Le}^{-2} b} + \left(\sigma + \frac{s}{\sigma}\right) \left(\frac{1}{b} + \frac{1}{\text{Le}^{-2} b}\right), \quad (9)$$

$$C = -\sigma(r_T - r_C) + \left(\sigma + \frac{s}{\sigma}\right), \quad (10)$$

and the other entries of the nontrivial fixed points are given in terms of the  $X$  entry as follows:

$$Y_0^{\pm, \mp} = \frac{r_T b X_0^{\pm, \mp}}{b + (X_0^{\pm, \mp})^2}, \quad (11)$$

$$Z_0^{\pm, \mp} = \frac{r_T (X_0^{\pm, \mp})^2}{b + (X_0^{\pm, \mp})^2}, \quad (12)$$

$$V_0^{\pm, \mp} = -\frac{X_0^{\pm, \mp}}{\sigma}, \quad (13)$$

$$W_0^{\pm, \mp} = \frac{r_C b \text{Le}^{-1} X_0^{\pm, \mp}}{b \text{Le}^{-2} + (X_0^{\pm, \mp})^2}, \quad (14)$$

$$U_0^{\pm, \mp} = \frac{r_C (X_0^{\pm, \mp})^2}{b \text{Le}^{-2} + (X_0^{\pm, \mp})^2}. \quad (15)$$

Among the four,  $\mathbf{X}_0^{+, +}$  and  $\mathbf{X}_0^{-, +}$  correspond to the two fixed points in the Lorenz system that undergo Hopf bifurcation. Hopf bifurcation can then be detected by examining the eigenvalues of the matrices representing the linearized system around these fixed points. The Hopf bifurcation curves plotted in the  $r_T$ - $s$  and  $r_T$ - $r_C$  spaces in this study are computed using this method. Note that the computation of the fixed points involves divisions by  $\text{Le}^{-1}$  with which it is implicitly assumed

that  $\text{Le}^{-1} > 0$ . The fixed points of smaller systems requiring  $\text{Le}^{-1} = 0$  such as that of Stenflo [1996] thus cannot be obtained using (7)–(15), but the computation must instead begin with the reduced system by setting  $r_C = \text{Le}^{-1} = 0$  in (1)–(6). In the Lorenz–Stenflo system, the four-tuple fixed points equivalent to the six-tuple nontrivial fixed points  $\mathbf{X}_0^{\pm, +}$  are given by  $\mathbf{X}_s^{\pm} = (\pm X_s, \pm Y_s, Z_s, \pm V_s)$ , where  $X_s = \sqrt{b Z_s / (1 + s/\sigma^2)}$ ,  $Y_s = \sqrt{b Z_s (1 + s/\sigma^2)}$ ,  $Z_s = r_T - 1 - s/\sigma^2$ , and  $V_s = -X_s/\sigma$  [Park *et al.*, 2015].

Heteroclinic bifurcation and the onset of chaos in the parameter spaces are detected numerically. The numerical solutions of the system are obtained using the fourth-order Runge–Kutta method with the integration time step size of  $\Delta\tau = 10^{-4}$ . In Lorenz and Lorenz-like systems, the global bifurcation incurring chaos typically involves the emergence of a chaotic trajectory coming from an initial condition around the trivial fixed point  $\mathbf{X}_0$ , but we also examine the trajectories associated with  $\mathbf{X}_0^{\pm, -}$  where applicable. In this study, the standard parameter values  $\sigma = 10$  and  $b = 8/3$  are used throughout. Whether the obtained numerical solutions are chaotic or nonchaotic can be decided algorithmically. Here, we use the peak-counting method based on [Dullin *et al.*, 2007]. In brief, the algorithm counts the number of repeated peaks, or the *period number*, in the time series of a solution for variable  $Z$ . Following Moon *et al.* [2019], we consider a numerical solution to be stable if its period number is zero and chaotic if its period number is  $\geq 8$ . A solution is  $n$ -periodic, if  $n$  number of peaks are repeated,  $1 \leq n < 8$ . Note that the algorithm is applied only after an ample amount of integration time ( $\tau \geq 400$ ) is given. This is because the type of attractor to which a solution ultimately converges can be unclear based on a short integration time, as exemplified by the well-known instances of transient chaos in the Lorenz system [Yorke & Yorke, 1979]. The six-dimensional system is also known to encounter at times a delayed emergence of chaos [Moon *et al.*, 2019]. The stability of periodic solutions in the sense of Floquet theory is ascertained following a numerical criterion similar to that suggested in [Seydel, 1987]. For this, Lyapunov exponents are estimated based on the Gram–Schmidt orthonormalization method [Christiansen & Rugh, 1997] using numerical solutions from 1000 randomly selected initial conditions belonging to the periodic attractor basin.

Given a parameter space, the approximate locations of bifurcation points where there occur transitions between different solution types can be detected by computing the peak number for the numerical solution corresponding to each of the points in the parameter space. In this way, the bifurcation curves marking the emergence of nonstable solutions are plotted in the  $r_T$ - $r_C$  and  $r_T$ - $s$  parameter spaces with the resolutions  $\Delta r_T = \Delta r_C = 0.1$  and  $\Delta s = 1$ . The same numerical integration and the peak-counting methods are also used to compute the basin boundaries in the phase space. The three-dimensional structures of the basin boundaries for the select parameter choices resulting in coexisting attractors are obtained from computing the peak number associated with each point in the  $X$ - $Y$ - $Z$  phase space with the resolution  $\Delta X = \Delta Y = \Delta Z = 1$ .

### 3. Results

#### 3.1. Effects of rotation only: The Lorenz–Stenflo case

We first study the effects of extending the Lorenz system by considering the effects of rotation only. This is achieved by setting  $r_C = \text{Le}^{-1} = 0$  in (1)–(6), which is equivalent to studying the Lorenz–Stenflo system because doing so decouples (5) and (6) from the rest of the system. In the context of Rayleigh–Bénard convection, the rotational parameter  $s$  is given so that it is proportional to the Taylor number,  $\text{Ta} = 4\Omega^2 H^4 / \nu_m^2$ , where  $\Omega$  is the angular velocity of rotation,  $H$  is the distance between the top and bottom boundaries, and  $\nu_m$  is the kinematic viscosity. In this view, raising  $s$  corresponds to intensifying the rotational effects.

The bifurcation structure of this reduced four-dimensional system in the  $r_T$ - $s$  space with the standard parameters is shown in Fig. 1. Figures 1(b) and 1(c) are sections of Fig. 1(a) magnified in the parameter windows containing select points corresponding to the trajectories plotted in Fig. 2. The Hopf bifurcation curve in Fig. 1(a) precisely matches the neutral stability curves for the Lorenz–Stenflo system reported in [Park et al., 2016]. The other two curves indicating the emergence of nonstable and chaotic solutions are also in agreement with the  $r_T$ - $s$  “periodicity diagram” from [Park et al., 2015], which shows the heteroclinic bifurcation coinciding with the emergence of chaos at low  $s$  ( $\lesssim 100$ ) and with periodicity at higher  $s$ . As can

be seen in Fig. 1, raising  $s$  results in increases in the critical thermal Rayleigh parameter  $r_T$  beyond which instability ensues.

Plotted together, the Hopf and heteroclinic bifurcation curves experience a slight mismatch at low  $s$  indicating the coexistence of chaotic and point attractors. When  $s = 0$ , the narrow gap located around  $r_T \approx 24$  confirms the previously reported  $r_T$  range of coexistence in the original Lorenz system [Yorke & Yorke, 1979]. The difference between these two bifurcation points in response to changing  $s$  initially exacerbates the mismatch between the two bifurcation curves as  $s$  is raised. Figure 1(c) shows that the coexistence region created by this gap continues to expand as  $s$  is further raised initially. In Fig. 2(b), the pair  $(r_T, s) = (39, 80)$ , which belongs to this coexistence gap, leads to a chaotic attractor represented by a trajectory starting near the trivial fixed point and two point attractors indicated by the inward-spiraling trajectories converging to the two nontrivial locally stable fixed points. The parameter combinations  $(r_T, s) = (40, 50)$  and  $(r_T, s) = (30, 80)$  are located outside of this coexistence region in Fig. 1(c):  $(r_T, s) = (40, 50)$  in the nonstable region and  $(r_T, s) = (30, 80)$  in the stable region. Corresponding to  $(r_T, s) = (40, 50)$ , Fig. 2(d) shows all three trajectories exhibiting chaos. Corresponding to  $(r_T, s) = (30, 80)$ , Fig. 2(f) shows all three trajectories being absorbed by one of the two nontrivial locally stable fixed points.

As  $s$  is further raised, the relative positions of the bifurcation curves in Fig. 1(a) start to become complicated starting with an inflection point on the heteroclinic bifurcation curves at  $(r_T, s) \approx (43.7, 111)$ . The complexity that follows is thought to be caused by the intermittency between the chaos-dominant instabilities at relatively low  $s$  ( $\lesssim 100$ ) and the periodicity-dominant instabilities at higher  $s$ , often found during a transition from one instability regime to another [Moon et al., 2019]. A portion of this region is shown in Fig. 1(b). Within this window, the curve indicating heteroclinic bifurcation stays to the left of the Hopf bifurcation curve, while the curve indicating the onset of chaos crosses the Hopf bifurcation curve twice, first going from the left to right between  $s = 115$  and  $s = 120$  and again coming back from the right to left between  $s = 125$  and  $s = 130$ , creating a diversity of situations for different coexistence phenomena depending on the relative positions of the parameter pairs with respect to the bifurcation curves. For example,



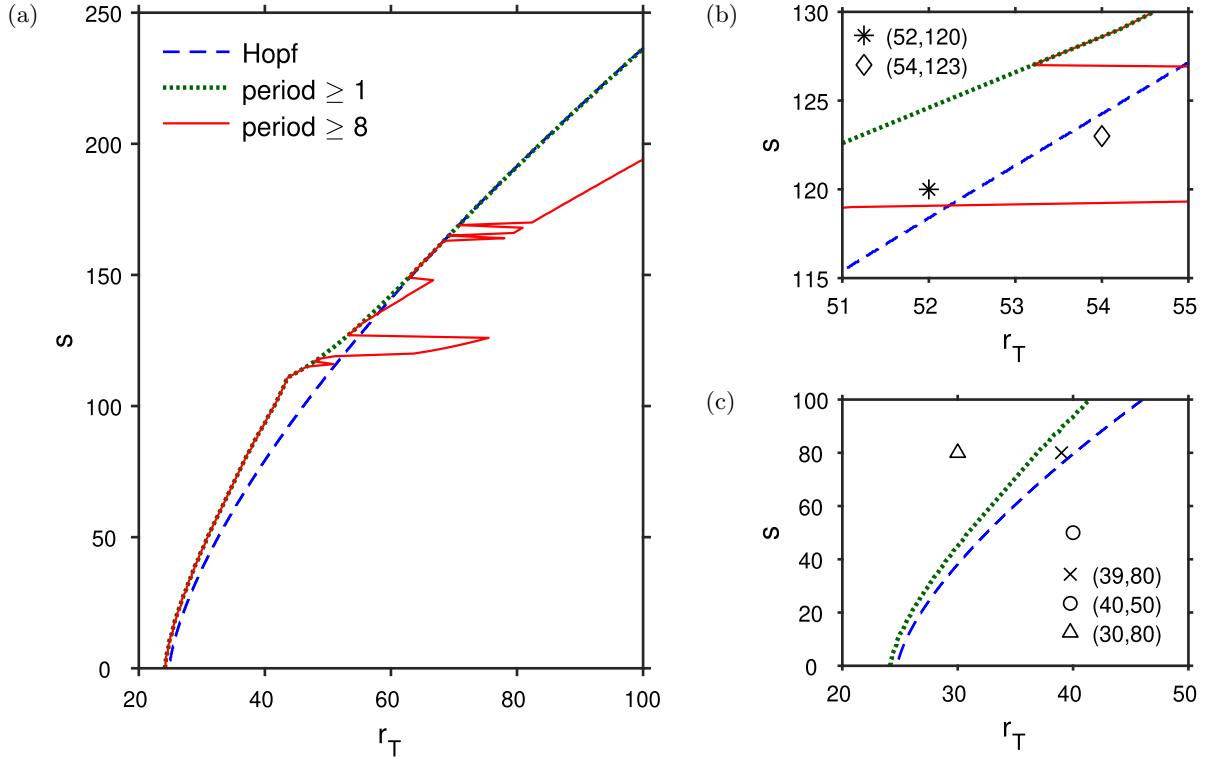


Fig. 1. Curves indicating Hopf bifurcation of  $\mathbf{X}_s^\pm$  (blue, dashed), the emergence of chaotic solutions (period number  $\geq 8$ ; red, solid), and the emergence of nonstable solutions (period number  $\geq 1$ ; green, dotted) in the Lorenz–Stenflo system (a) on the  $r_T$ - $s$  space and (b) and (c) the magnified portions of the parameter space containing selections of parameter points for the trajectories plotted in Fig. 2. Note that the bifurcations occur as the curves are crossed from the left to right, that is, as  $r_T$  is increased for any given  $s$ . In (c), the bifurcation curves for period number  $\geq 1$  and for period number  $\geq 8$  overlap completely, so only the former is shown (green, dotted).

at  $(r_T, s) = (52, 120)$ , initial conditions near the trivial fixed point are expected to yield nonstable yet nonchaotic trajectories because this  $r_T$ - $s$  pair [ $*$  in Fig. 1(b)] is located to the right of the curve indicating the emergence of nonstable solutions but has not crossed the curve indicating the emergence of chaos. On the other hand, the initial conditions near the nontrivial fixed points are expected to still yield stable solutions as  $(r_T, s) = (52, 120)$  is still located to the left of the Hopf bifurcation curve. Indeed, the corresponding trajectories in Fig. 2(a) for  $(r_T, s) = (52, 120)$  exhibit the coexistence of 2-periodic (largest Lyapunov exponent  $\sim 0.009$ ) and stable solutions.

The location of the pair  $(r_T, s) = (54, 123)$  relative to the bifurcation curves [ $\diamond$  in Fig. 1(b)] is even more peculiar in that the Hopf bifurcation is expected to have occurred already, but chaos still has not emerged. Figure 2(c) for  $(r_T, s) = (54, 123)$  shows that at  $\tau = 20$ , a periodic trajectory (largest Lyapunov exponent  $\sim 0.01$ ) has emerged from the

trivial fixed point while the trajectories starting near the nontrivial fixed points seem to slowly spiral away from those nontrivial fixed points. Further integrating up to  $\tau = 100$ , it is observed in Fig. 2(e) that the trajectories from the nontrivial fixed points continue to spiral out, eventually settling on the periodic orbit. The situation at  $(r_T, s) = (54, 123)$  is a periodic analogue of Fig. 2(d), where there is no coexistence of different attractor types. Instead of chaos, all points in the phase space, except for the fixed points and their stable manifolds, lead to periodicity in Figs. 2(c) and 2(e). In such situations, the entire phase space would belong to the same periodic basin, neglecting the stable manifolds of the fixed points and the possibility of a hidden basin of attraction. This is why in Fig. 3 we focus on the basins of attraction corresponding to different types of attractors.

The three-dimensional shapes of the basin boundaries are plotted in Fig. 3 for select parameter choices resulting in coexisting attractors in

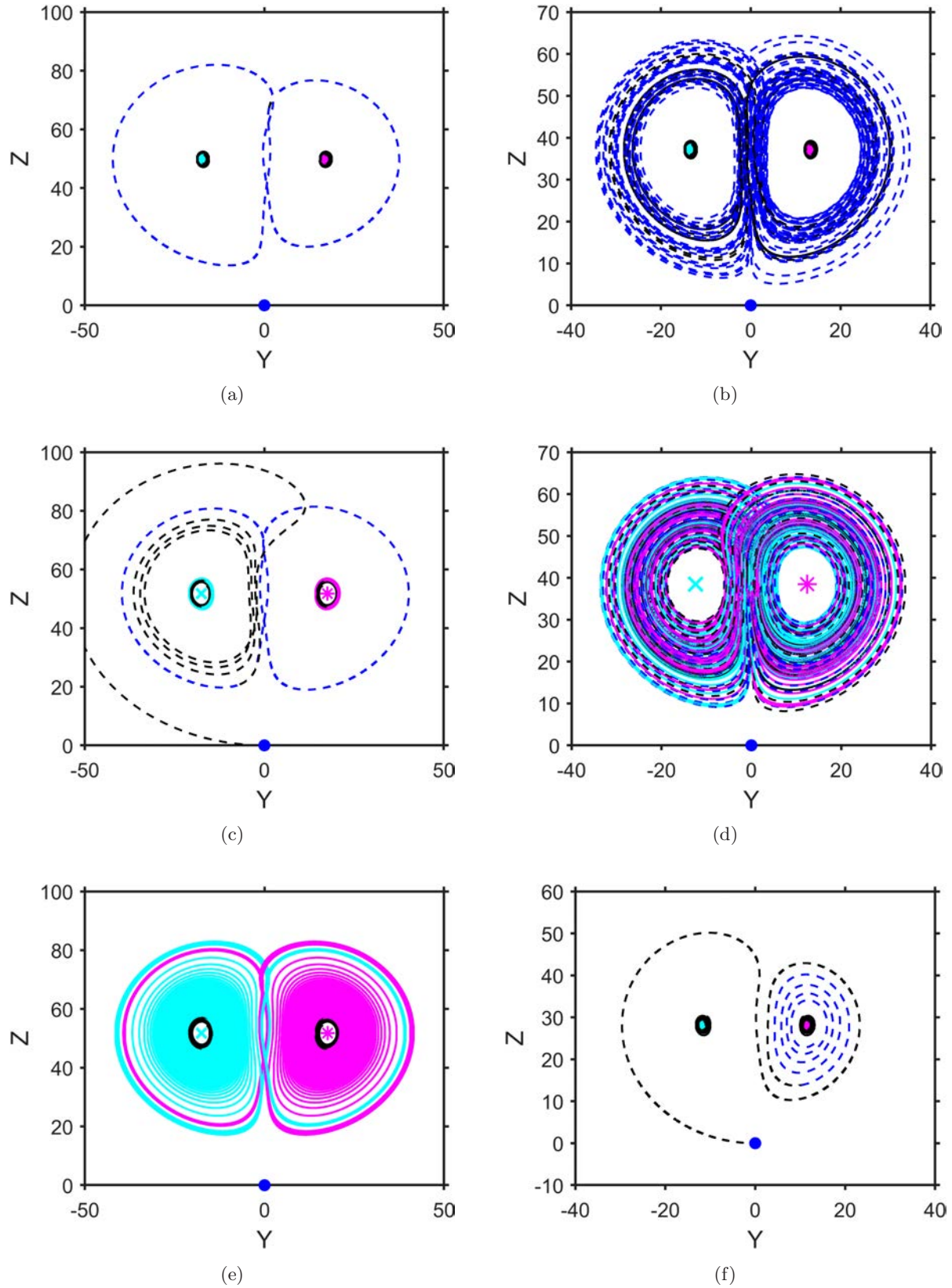


Fig. 2. Trajectories demonstrating the occurrences and absence of coexisting attractors in the Lorenz–Stenflo system with (a)  $(r_T, s) = (52, 120)$ , (b)  $(r_T, s) = (39, 80)$ , (c)  $(r_T, s) = (54, 123)$  up to  $\tau = 20$ , (d)  $(r_T, s) = (40, 50)$ , (e)  $(r_T, s) = (54, 123)$  up to  $\tau = 100$  and only for the nontrivial fixed points, and (f)  $(r_T, s) = (30, 80)$ . Each of the trajectories starts out black and switches over to the color matching the fixed point it is associated with: cyan for  $\mathbf{X}_0^{-,+}$ , magenta for  $\mathbf{X}_0^{+,+}$ , and blue for  $\mathbf{X}_0$ .

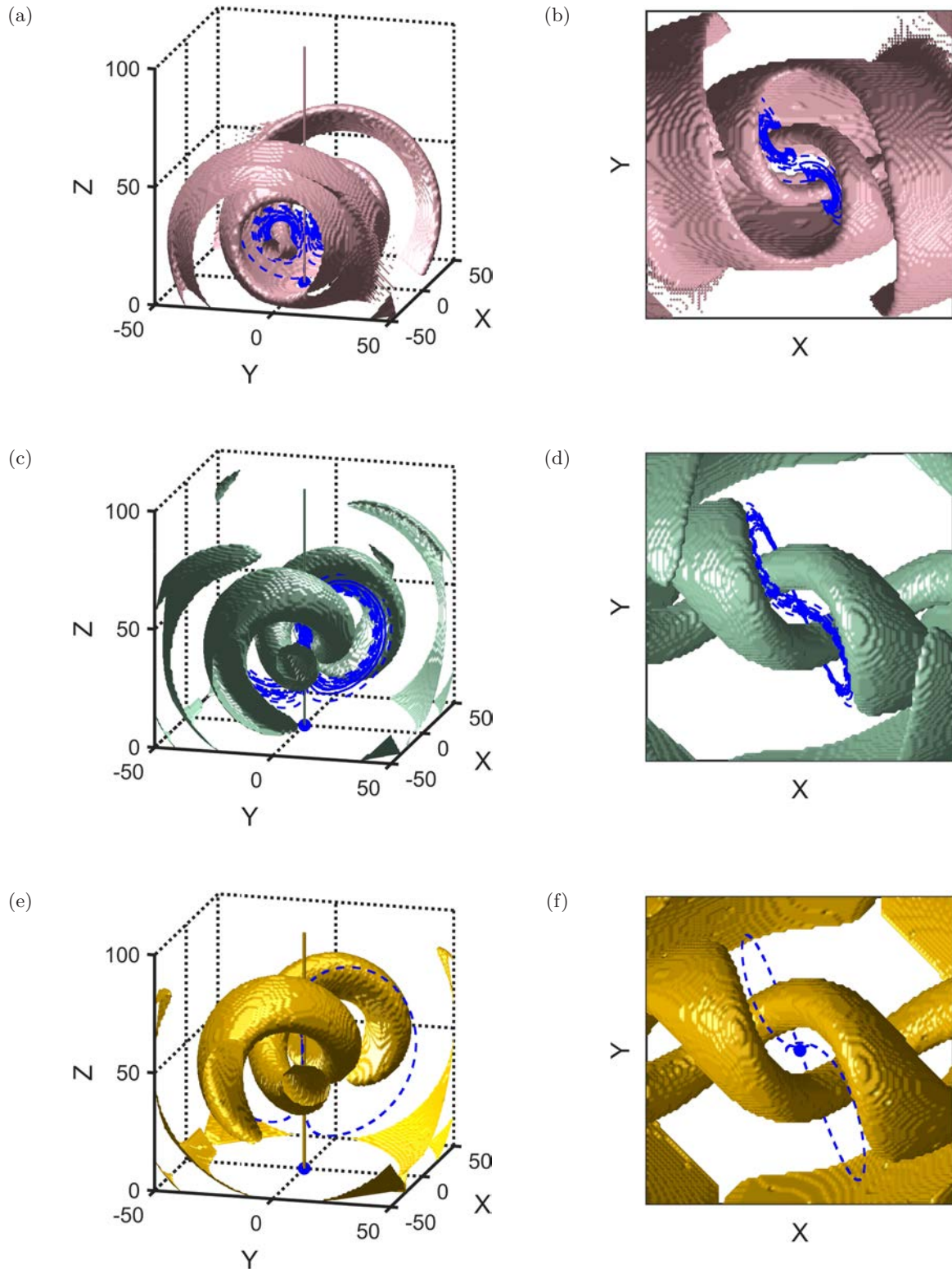


Fig. 3. Boundary surface in the  $X$ - $Y$ - $Z$  space between (a) chaotic and point attractor basins along with the chaotic trajectory starting near the trivial fixed point (blue) of the three-dimensional Lorenz system with  $r_T = 24.4$ , (c) chaotic and point attractor basins along with the chaotic trajectory starting near the trivial fixed point (blue) of the Lorenz-Stenflo system with  $r_T = 39$  and  $s = 80$ , and (e) periodic and point attractor basins along with the periodic trajectory starting near the trivial fixed point (blue) of the Lorenz-Stenflo system with  $r_T = 52$  and  $s = 120$ . Subfigures (b), (d), and (f) show, respectively, (a), (c), and (e) viewed from the top at  $Z = 100$ .



the Lorenz and Lorenz–Stenflo systems. No hidden basin has been found in the three cases. Figures 3(a) and 3(b) show the boundary between the coexisting chaotic and point attractor basins for the three-dimensional Lorenz system with  $r_T = 24.4$ ,  $\sigma = 10$ , and  $b = 8/3$ . Figures 3(c) and 3(d) show the chaotic–point attractor basin boundary like in Figs. 3(a) and 3(b) but for the Lorenz–Stenflo system with  $r_T = 39$  and  $s = 80$ , corresponding to the situation in Fig. 2(b).

In Fig. 3(a), the point attractor basin for the three-dimensional Lorenz system forms a relatively thin pipe-like structure twisting around  $X = Y = 0$  close to the center of the chaotic attractor and a shell-like outer structure twirling around a horizontal axis parallel to the  $Y = Z = 0$  line. This horizontal axis, indicative of the location of the attractor in the  $Z$ -direction, hovers atop the  $Z = 0$  plane and is located at  $Z \approx 35$  in Fig. 3(a) and higher in Figs. 3(c) and 3(e). For the remainder of this paper, we refer to this imagined horizontal line as the *horizontal axis of twirling*. More precisely, let  $Z_{\text{center}} = 0.5(Z_{\text{max}} + Z_{\text{min}})$  be the midpoint between the maximum,  $Z_{\text{max}}$ , and minimum,  $Z_{\text{min}}$ , of the numerical solution for  $Z$  over  $\tau \in [200, 250]$ . Then  $(X, Y, Z) = (0, 0, Z_{\text{center}})$  is located roughly at the center of each attractor. For the attractors corresponding to the conditions for Figs. 3(a), 3(c), and 3(e),  $Z_{\text{center}}$  indeed increases from  $\sim 34.3$  to  $\sim 57.6$  and to  $\sim 79.3$ , respectively.

The pipe-like structure of the point attractor basin for the Lorenz–Stenflo system shown in Figs. 3(c) and 3(d) exhibits a twisting similar to that in Figs. 3(a) and 3(b) but with thicker pipes and a loosened grip around the horizontal axis of twirling. Measured across the  $Y$  direction at  $(X, Z) = (0, Z_{\text{center}})$ , the diameter  $\delta_Y$  of the pipes in the vicinity of  $Z_{\text{center}}$  in the  $Y$  direction is about  $8\Delta Y$  for Figs. 3(a) and 3(b) and about  $9\Delta Y$  for Figs. 3(c) and 3(d). Even as the horizontal axis of twirling shifts upward going from Figs. 3(a) to 3(c), the loosened grip creates large gaps between the outer layers of the point attractor basin, pushing the bottom part of the twirling shell-like structure below the  $Z = 0$  plane. This is why the bottom layer of the basin boundary is captured within  $Z \in [0, 100]$  in Fig. 3(a) and is also visible in Fig. 3(b) but not in Figs. 3(c) and 3(d). The boundary between the coexisting periodic and point attractor basins for the Lorenz–Stenflo system with  $r_T = 52$  and  $s = 120$  in Figs. 3(e)

and 3(f) corresponding to the situation depicted by Fig. 2(a) exhibits similar characteristics as that between the chaotic and point attractor basins in Figs. 3(c) and 3(d) but with an even more loosened grip around an even higher horizontal axis of twirling.

A rough estimate of how loose a grip is around the horizontal axis can be obtained from comparing the volumes of the basins under consideration in the  $X$ – $Y$ – $Z$  space. Since the horizontal axis of twirling shifts upward going from Figs. 3(a) to 3(c) and to 3(e), a fairer comparison can be made by considering the rectangular cuboid containing only the top half of each attractor, that is,  $X \times Y \times Z$  with  $X, Y \in [-50, 50]$  and  $Z \in [Z_{\text{center}}, Z_{\text{max}}]$ . The estimated volume ratio  $\mathcal{V}_{\text{nonstable}}/\mathcal{V}_{\text{total}}$ , where  $\mathcal{V}_{\text{nonstable}}$  is the volume of the nonstable basin within this cuboid and  $\mathcal{V}_{\text{total}}$  is the total volume of the cuboid containing the top half of each attractor, is slightly higher for Fig. 3(e) at  $\sim 0.86$  than for Fig. 3(c) at  $\sim 0.79$  despite the former having thicker pipes whose diameters are measured to be about  $10\Delta Y$ . Such a volume ratio can be interpreted as the likelihood that a randomly chosen initial condition would fall into a nonstable basin of attraction. Note that the provided ratios are computed using the volumes estimated with the grid resolution of  $\Delta X = \Delta Y = \Delta Z = 1$ . The volume ratio is relatively high for Fig. 3(a) at  $\sim 0.82$ , but this is attributed to the stable basin in Fig. 3(a) having thinner pipes compared to the other two cases. Indeed, the product  $(\mathcal{V}_{\text{nonstable}}/\mathcal{V}_{\text{total}})\delta_Y$  of the volume ratio and the estimated diameter is highest for Fig. 3(e) at  $\sim 8.66$  followed by that for Fig. 3(c) at  $\sim 7.17$  and then by Fig. 3(a) at  $\sim 6.62$ , in agreement with the above assessment.

The changes in the heights of the horizontal axes of twirling seem to mainly reflect the effects of increased  $r_T$ , going from 24.4 in Fig. 3(a) to 52 in Fig. 3(e). It was reported in [Moon et al., 2019] that, all else being equal, raising  $r_T$  has the effect of making the chaotic attractor larger and levitate higher up above the  $Z = 0$  surface. The loosening grip of twirling appears to be associated with the rising  $s$  going from 0 to 80 and then to 120 in Figs. 3(a), 3(c), and 3(e), respectively. Furthermore, raising  $s$  to such levels appears to bring the system toward the center of the chaotic region in the  $r_T$ – $s$  parameter space [Park et al., 2015], which might result in a larger chaotic basin and thus loosening of the grip around the twirling axis. It is noted that still



further investigation is needed to provide explanations for and implications of the observed effects of the parameters, particularly in the context of various applications including nonlinear dynamics of thermal convection.

### 3.2. Simultaneous effects of rotation and scalar

We now study coexisting attractors in the full six-dimensional system (1)–(6) considering the simultaneous effects of both the rotational parameter  $s$  and the scalar-related parameter  $r_C$ . In the derivation of (1)–(6), the density-affecting scalar is assumed to negatively influence buoyancy [Moon *et al.*, 2019]. For this reason, while the Rayleigh-type parameter  $r_C$  is formulated similarly to the Rayleigh parameter  $r_T$ , the two parameters are expected to exert opposite effects on the stability of the system. Scaled properly, as in Fig. 4, the competition between the stabilizing effects of  $r_C$  and the destabilizing effects of  $r_T$  can be captured [Veronis, 1968] similar to the more conventional  $r_T$ – $s$  and  $r_T$ – $\sigma$  parameter spaces [Bykov & Shilnikov, 1992; Park *et al.*, 2015]; however, note that even though the two additional ingredients both have stabilizing effects, the details of how the system responds to increases in  $r_C$  and  $s$  and how it ultimately reaches a stable state can be quite different. For example, Lyapunov exponent analyses with certain parameter combinations reveal that unlike raising  $s$ , which quickly neutralizes chaos and stabilizes the system, raising  $r_C$  can lead to lukewarm results, with the system alternating between stability and periodicity and eventually leading to the so-called “second-onset of chaos” for high  $r_C$  before ultimately stabilizing for good [Moon *et al.*, 2019].

Figure 4(a) shows the bifurcation structure in the  $r_T$ – $r_C$  space with the effects of rotation included (i.e.  $s \neq 0$ ), and Fig. 4(b) shows that with the effects of rotation excluded (i.e.  $s = 0$ ). The bifurcation curves in Fig. 4 show similar characteristics as those from Fig. 1 except there are mismatches between the Hopf bifurcation curves and the curves indicating the emergence of periodicity at relatively high  $r_C \gtrsim 2$ . It seems that for the case when  $s = 0$ , Hopf bifurcation continues to appear at higher  $r_T$  than the emergence of instability in trajectories starting near the trivial fixed point, even as the first emergence of nonstable solutions undergoes transitions from chaos to periodicity at higher  $r_C$ . Interestingly,

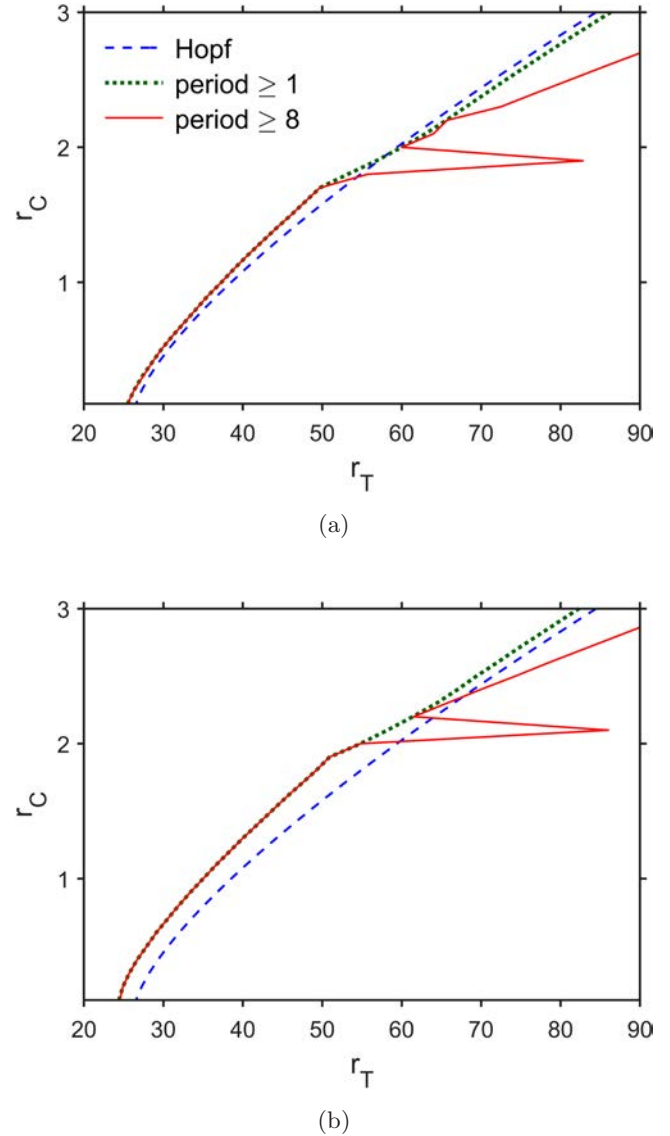


Fig. 4. Curves indicating Hopf bifurcation of  $\mathbf{X}_0^{\pm,+}$  (blue, dashed), the emergence of chaotic solutions (period number  $\geq 8$ ; red, solid), and the emergence of nonstable solutions (period number  $\geq 1$ ; green, dotted) in the six-dimensional system with  $\text{Le}^{-1} = 10$  and (a)  $s = 10$  and (b)  $s = 0$ .

when  $s = 10$ , the order in which the two bifurcations occur flips so that Hopf bifurcation is incurred prior to the heteroclinic bifurcation as  $r_T$  is raised.

Another source of complication may arise from having the two additional nontrivial fixed points  $\mathbf{X}_0^{\pm,-}$ , whose effects on the six-dimensional system’s stability and bifurcation structure have yet to be fully uncovered. To see whether the fixed points  $\mathbf{X}_0^{\pm,-}$  are real in this case, the numerator  $\mathcal{D}(r_T, r_C) \equiv -B - \sqrt{B^2 - 4AC}$  from (7) is plotted as a function of  $r_T$  and  $r_C$  in Fig. 5(a) with  $\text{Le}^{-1} = s = 10$ . Since  $\mathcal{D} < 0$  for all  $r_T$  and  $r_C$

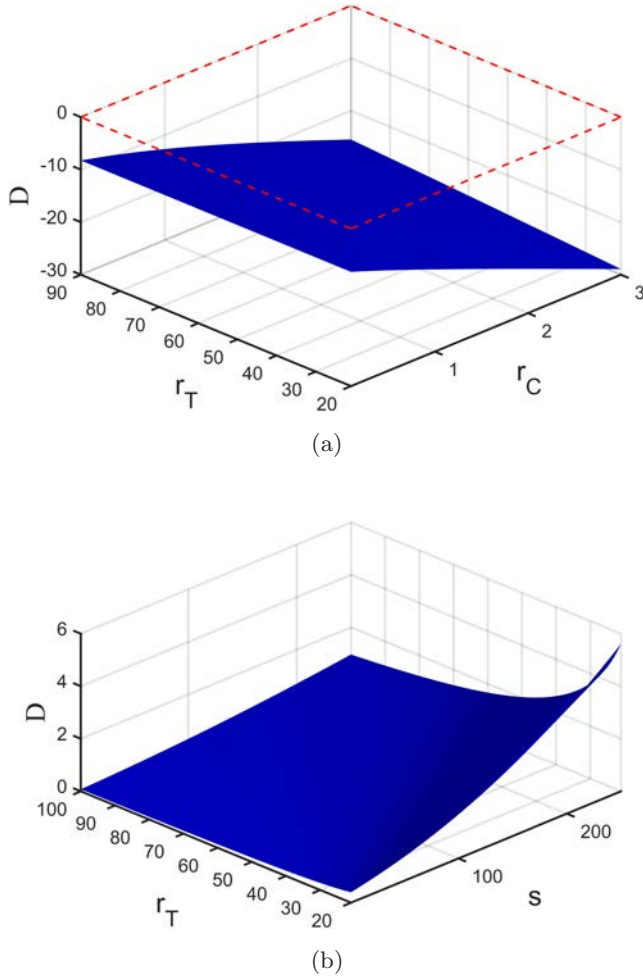


Fig. 5. Surface of  $\mathcal{D} = -B - \sqrt{B^2 - 4AC}$  from (7) as a function of (a)  $r_T$  and  $r_C$  with  $\text{Le}^{-1} = s = 10$ , corresponding to Fig. 4(a) and (b)  $r_T$  and  $s$  with  $r_C = r_T$  and  $\text{Le}^{-1} = 0.1$ , corresponding to Fig. 8(a). In (a), the  $\mathcal{D} = 0$  plane is highlighted by the red dashed edges.

in the parameter space window shown in Fig. 4(a) and  $A > 0$  always, the two additional fixed points do not reside in a real space  $\mathbb{R}^n$ . The fixed points  $\mathbf{X}_0^{\pm,-}$ , therefore, do not exist in the  $X$ - $Y$ - $Z$  phase space in which our analyses have been made thus far; nevertheless, since it is also known that initial conditions near complex fixed points can lead to interesting dynamics [Pham *et al.*, 2014], the real parts of the complex fixed point  $\mathbf{X}_0^{+,-}$  and the trajectories starting near the complex fixed point are plotted in Fig. 6 in addition to the trajectories starting near the real fixed points.

Figures 6(a), 6(c), and 6(e) on the left column of Fig. 6 show the phase space at various points of the parameter space corresponding to Fig. 4(a): where there is coexistence of chaotic and point attractors

[Fig. 6(a)], where all real fixed points lead to chaotic trajectories [Fig. 6(c)], and where all initial conditions in the real space lead to one of the two 1-periodic orbits on either side of  $Y = 0$  [Fig. 6(e)]. Ignoring for now the trajectories associated with complex fixed points, the conditions for the types of coexistence in display in Fig. 6 are the same as in Fig. 2. The coexistence of chaotic-stable solutions are found in the gap between Hopf bifurcation and the emergence of chaos [Fig. 6(a)]. After the real nontrivial fixed points undergo Hopf bifurcation as  $r_T$  is further raised, crossing the Hopf bifurcation curve in Fig. 4(a), only chaotic solutions remain [Figs. 6(c) and 6(d)]. The situation in Fig. 6(e) is similar to that in Fig. 2(c) in terms of the number of different solution types, except here we now have the coexistence of two separated periodic orbits around the real nontrivial locally unstable fixed points.

The three-dimensional shape of the boundary between the basins of these two periodic attractors featured in Fig. 6(e) is plotted in Figs. 7(c) and 7(d) along with relevant trajectories and fixed points. Notice how the basin boundary shown in Figs. 7(c) and 7(d) crosses the  $X$ - $Y$  plane in close proximity to the trivial fixed point  $\mathbf{X}_0$ , which suggests that depending on the precise initial condition, a trajectory from around the trivial fixed point can either go toward the attractor associated with  $\mathbf{X}_0^{+,+}$  [magenta, \* in Figs. 6(e), 7(c) and 7(d)] or that with  $\mathbf{X}_0^{-,+}$  (cyan,  $\times$ ). In the particular case shown in Figs. 6(e), 7(c), and 7(d), the trajectory corresponding to the trivial fixed point has an initial condition belonging, albeit by only a small margin, to the basin associated with  $\mathbf{X}_0^{-,+}$ , and so it is attracted to the periodic orbit associated with  $\mathbf{X}_0^{-,+}$ , that is, to the left of  $Y = 0$  in Fig. 6(e).

Each of the figures in the right column of Fig. 6 reveals what happens before leading up to the state of the trajectories displayed in Fig. 6(a), 6(c), or 6(e) to its left. Note that in all three cases, the trajectories starting near the complex fixed point are periodic, although some can traverse wide swaths of the phase space or leave behind intricate trails before landing on periodic orbits [i.e. Figs. 6(b) and 6(f)]. Sometimes, for example in Fig. 6(c), the periodic orbit coming from the complex fixed point covers such a wide area that the chaotic attractor is barely visible in the  $Y$ - $Z$  window zoomed out to capture the entirety of the periodic orbit.

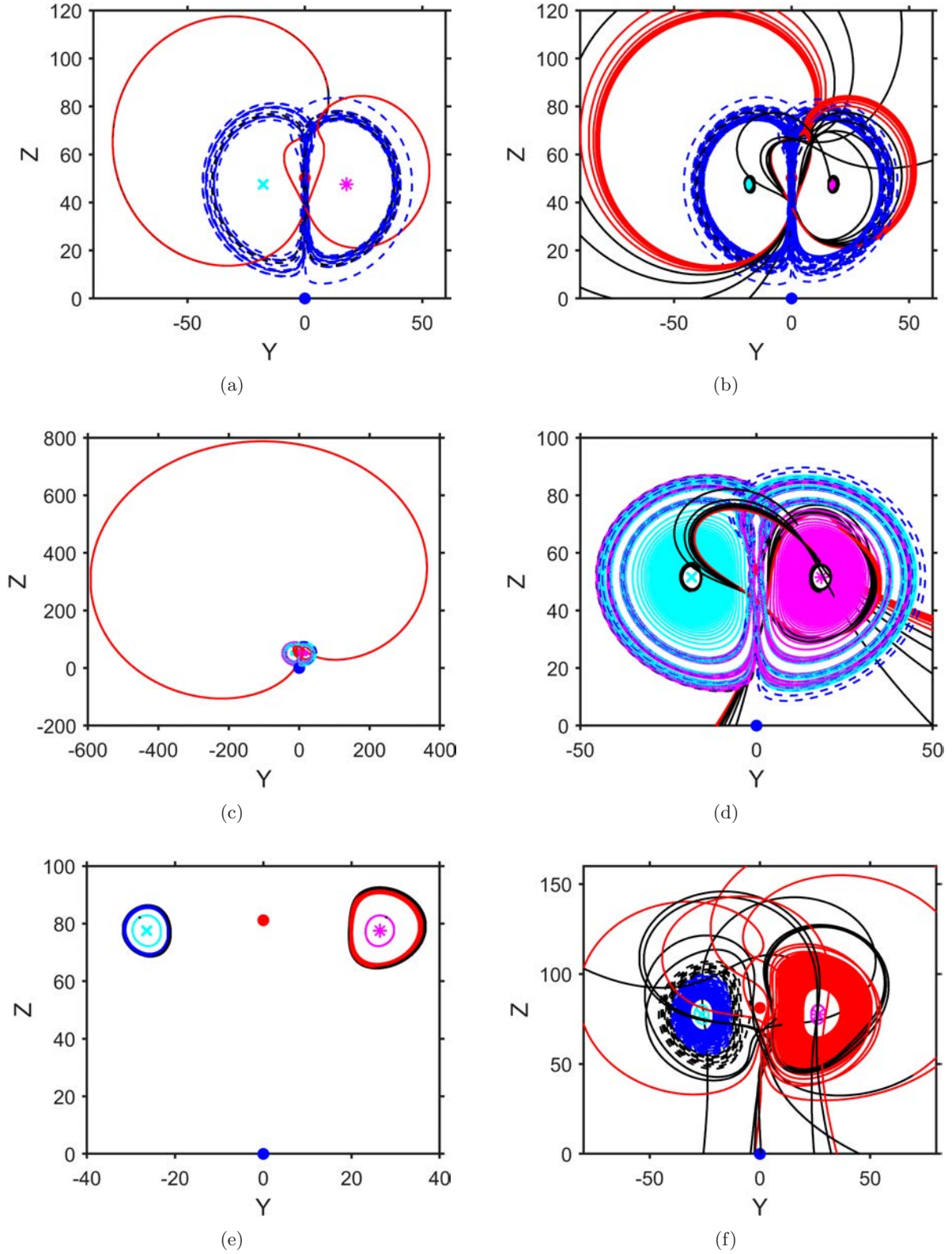


Fig. 6. Trajectories of the solutions from  $\tau = 70$  to  $\tau = 100$ , corresponding to selected points from Fig. 4(a) with (a)  $(r_T, r_C) = (50, 1.65)$ , (c)  $(r_T, r_C) = (54, 1.65)$ , and (e)  $(r_T, r_C) = (80.9, 2.8)$  projected on the  $Y$ - $Z$  plane. Subfigures (b), (d), and (f) show the trajectories of the same solutions as (a), (c), and (e), respectively, but from  $\tau = 0.5$  to  $\tau = 75$ . The points consisting of the real parts of the respective entries of the complex fixed point  $\mathbf{X}_0^{+,-}$  are also plotted (red) on the  $Y$ - $Z$  planes along with the trajectories starting nearby. The colors switch from black to those matching the corresponding fixed points after five time units into the numerical integrations.



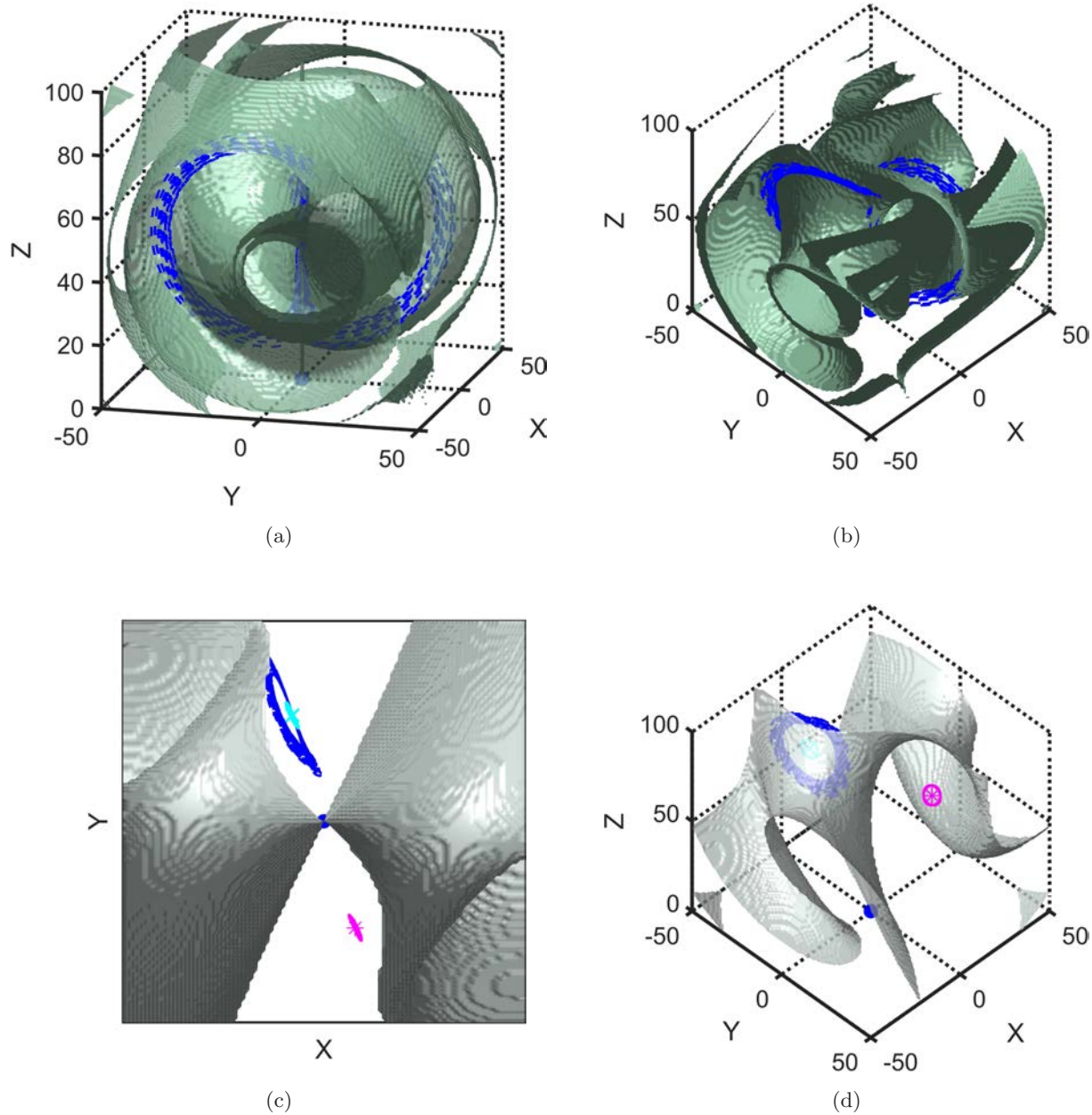


Fig. 7. Boundary surface in the  $X$ - $Y$ - $Z$  space between chaotic and point attractor basins corresponding to Fig. 6(a) along with the chaotic trajectory starting near the trivial fixed point (blue) of the six-dimensional system with  $r_T = 50$ ,  $r_C = 1.65$ , and  $s = Le^{-1} = 10$  viewed from (a) a 15° angle and (b) a 45° angle with trimmed outer layers. The boundary surface between the basins associated with the two periodic attractors of the six-dimensional system with  $r_T = 80.9$ ,  $r_C = 2.8$ , and  $s = Le^{-1} = 10$  corresponding to Fig. 6(e) along with the trajectories from the trivial fixed point (blue) and those associated with the two real nontrivial fixed points (cyan and magenta) viewed from (c) the top at  $Z = 100$  and (d) a 45° angle.

Since these periodic orbits are associated with complex fixed points, no basins for these periodic orbits are found in the real attractor basins computed for Figs. 7(a) and 7(b) corresponding to the point  $(r_T, r_C) = (50, 1.65)$  and Fig. 6(a), but only the boundary between chaotic and point attractor basins is found. Notice how the phase space in

Fig. 7(a) is so tightly packed with thick pipes consisting of the point attractor basin that some of the outer shells had to be trimmed in Fig. 7(b) in order to be able to properly inspect the basin structure. The stabilizing effects of  $r_C$  may have contributed to this thickening of the point attractor basin. The tight packing of the phase space is also influenced



by an intensified twirling of the outer shell-like layers of the basin, which may be attributed to the relatively low  $s$  at 10.

To see the effects of having two additional real nontrivial fixed points, the case when  $r_T = r_C$  and  $\text{Le}^{-1} = 0.1$  is considered for Fig. 8. As shown in Fig. 5(b),  $\mathcal{D}(r_T, s)$  in this case is always positive inside the  $r_T$ - $s$  window considered, so  $\mathbf{X}_0^{\pm,-}$  are real. Here, a relatively small  $\text{Le}^{-1}$  is chosen so that  $B < 0$  from (9), and  $r_C = r_T$  is chosen to simplify the parameter choices. We focus on the  $r_T$ - $s$

parameter space for a straightforward comparison against the Lorenz–Stenflo case in Fig. 1.

In addition to the Hopf bifurcation curve, Figs. 8(a) and 8(b) plot the heteroclinic bifurcation curves marking the emergence of nonstable solutions in the trajectories starting near the trivial and near the additional nontrivial fixed point  $\mathbf{X}_0^{+,-}$ . The emergence of chaos occurs almost simultaneously for the trajectories associated with these two fixed points, and they are barely distinguishable even when magnified in Fig. 8(b). The precise moment

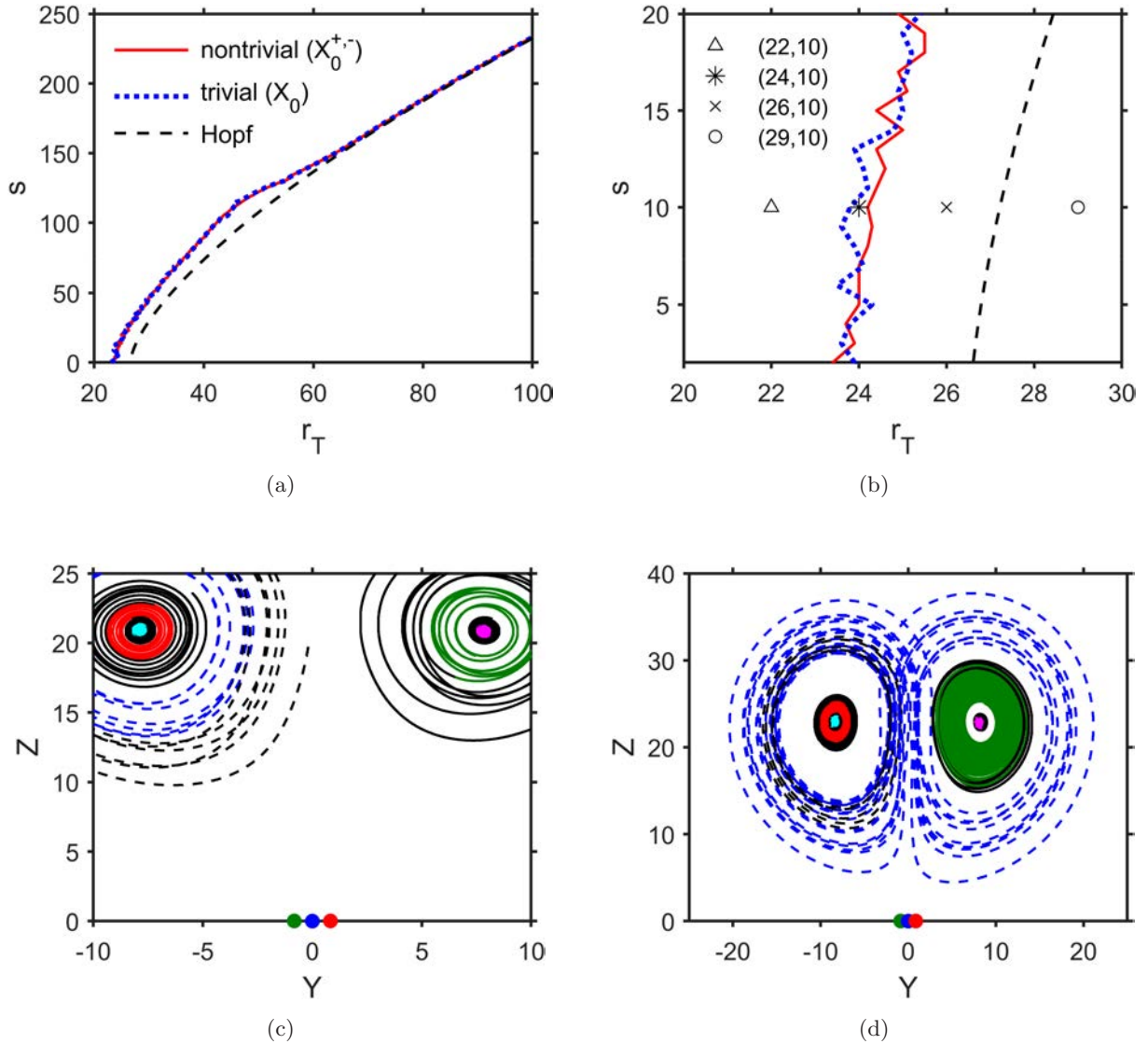


Fig. 8. Curves indicating Hopf bifurcation of  $\mathbf{X}_0^{\pm,+}$  (black, dashed), the emergence of nonstable solutions (period number  $\geq 1$ ) starting near the trivial fixed point  $\mathbf{X}_0$  (blue, dotted) and in the solutions starting near the fixed point  $\mathbf{X}_0^{+,-}$  (red, solid) for the six-dimensional system with  $r_C = r_T$  and  $\text{Le}^{-1} = 0.1$  in (a) the  $r_T$ - $s$  space and (b) a magnification window of the parameter space showing select parameter combinations corresponding to the trajectories in (c) for  $(r_T, s) = (22, 10)$ , (d) for  $(r_T, s) = (24, 10)$ , (e) for  $(r_T, s) = (26, 10)$ , and (f) for  $(r_T, s) = (29, 10)$ , color-coded in the same way as in Fig. 6 with an additional color (green) for the nontrivial fixed point  $\mathbf{X}_0^{+,-}$ .

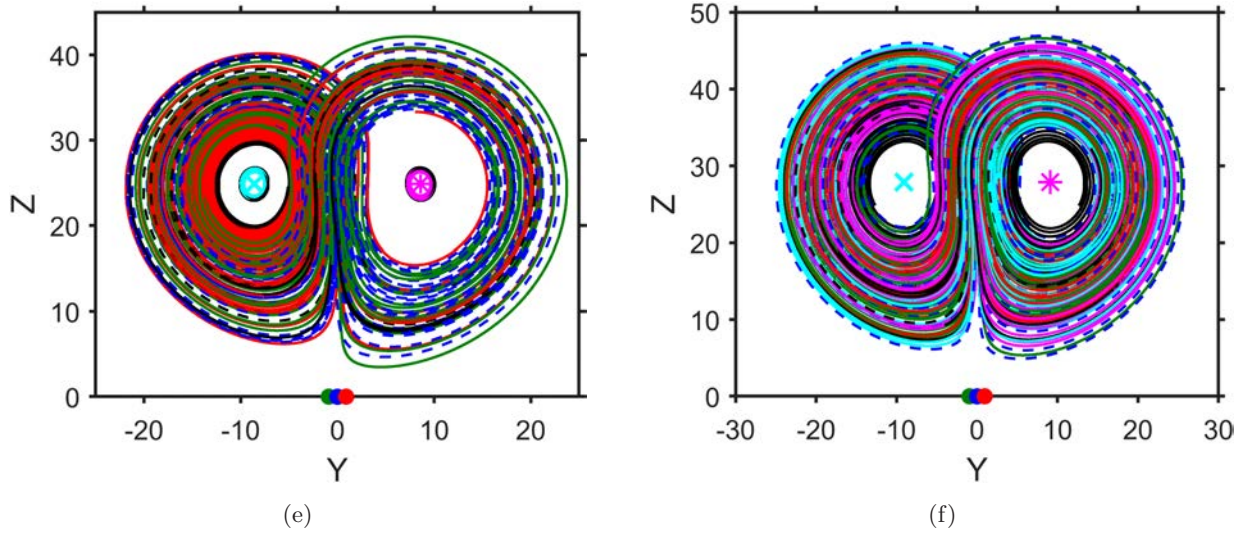


Fig. 8. (Continued)

of the emergence of chaos is somewhat unreliable according to these bifurcation curves and seems to be highly sensitive to the initial condition because there are three fixed points  $\mathbf{X}_0$ ,  $\mathbf{X}_0^{+,-}$ , and  $\mathbf{X}_0^{-,-}$  that sometimes sit very closely together. For example, even though the location of the pair  $(r_T, s) = (24, 10)$  between the two heteroclinic bifurcation curves suggests that the solutions with the initial conditions near the trivial fixed point are nonstable and those from near  $\mathbf{X}_0^{+,-}$  are stable, the seemingly chaotic trajectory from near the trivial fixed point in Fig. 8(d) corresponding to  $(r_T, s) = (24, 10)$  is in fact merely transiently chaotic in the sense of the “metastable chaos” from [Yorke & Yorke, 1979].

The positions of the other points in the  $r_T$ - $s$  parameter space relative to the bifurcation curves still reliably predict the possible coexistence or non-coexistence of attractors. Moving rightward from  $(r_T, s) = (22, 10)$  to  $(r_T, s) = (26, 10)$ , and to  $(r_T, s) = (29, 10)$ , there appear as expected two point attractors consisting of the locally stable non-trivial fixed points [Fig. 8(c)], the coexistence of chaotic and point attractors [Fig. 8(e)], and chaos after the Hopf bifurcation [Fig. 8(f)]. The seemingly inseparable chaotic trajectories associated with the three fixed points  $\mathbf{X}_0$ ,  $\mathbf{X}_0^{+,-}$ , and  $\mathbf{X}_0^{-,-}$  together with the close alignment of the two heteroclinic bifurcation curves in Fig. 8(b) plotted using the two fixed points suggest the possibility that all three of these fixed points might belong to the same basin of attraction for a single chaotic attractor shown in Fig. 8(f). That would mean that the two heteroclinic bifurcation curves in Fig. 8(b) are in fact

markings of the same global bifurcation and the differences are merely numerical. It remains open whether the statements above hold for all situations when  $\mathbf{X}_0^{\pm,-}$  are real.

#### 4. Summary and Conclusion

By superposing different bifurcation curves in parameter spaces, the conditions for coexisting attractors in the physically extended Lorenz systems are identified. It was revealed that the physically extended Lorenz system can exhibit other kinds of coexistence such as coexistence of periodic and point attractors or that of two different periodic orbits in addition to the well-known coexistence of chaos and stability just before the Hopf bifurcation of the nontrivial fixed points in the original Lorenz system. The basins of attraction in the phase space are computed for select representative cases, and their three-dimensional shapes are rendered in the  $X$ - $Y$ - $Z$  phase space. The relationship between the parameters and the coexisting basins of attraction needs more in-depth research; for example, there appears to be a relationship between the rotational parameter  $s$  and the intensity of twirling in the outer shell-like structure of the basin boundaries.

It might be possible to gain some fundamental insights about atmospheric predictability from studying coexisting attractors in the physically extended Lorenz system. For instance, given a solution from an initial condition near a boundary between coexisting attractor basins, a small change in the initial condition can lead to a qualitative

change in the solution characteristics. Such sensitive dependence of solution characteristics on initial conditions near the basin boundaries can have conceptually important implications regarding the predictability of weather and climate.

## Acknowledgments

The authors are grateful to two anonymous reviewers for helpful comments and suggestions. This work was supported by the Small Grant for Exploratory Research (SGER) program through the National Research Foundation of Korea (NRF-2018R1D1A1A02086007).

## References

- Argyris, J. & Andreadis, I. [2000] "On the influence of noise on the coexistence of chaotic attractors," *Chaos Solit. Fract.* **11**, 941–946.
- Bashkirtseva, I. & Ryashko, L. [2009] "Constructive analysis of noise-induced transitions for coexisting periodic attractors of the Lorenz model," *Phys. Rev. E* **79**, 041106.
- Bykov, V. V. & Shilnikov, A. L. [1992] "On the boundaries of the domain of existence of the Lorenz attractor," *Selecta Math. Sov.* **11**, 375–382.
- Christiansen, F. & Rugh, H. H. [1997] "Computing Lyapunov spectra with continuous Gram–Schmidt orthonormalization," *Nonlinearity* **10**, 1063–1072.
- Doedel, E. J., Krauskopf, B. & Osinga, H. M. [2006] "Global bifurcations of the Lorenz manifold," *Nonlinearity* **19**, 2947–2972.
- Dullin, H. R., Schmidt, S., Richter, P. H. & Grossmann, S. K. [2007] "Extended phase diagram of the Lorenz model," *Int. J. Bifurcation and Chaos* **17**, 3013–3033.
- Huang, Z., Cao, J. & Jiang, T. [2014] "Dynamics of stochastic Lorenz–Stenflo system," *Nonlin. Dyn.* **78**, 1739–1754.
- Li, C. & Sprott, J. C. [2014] "Multistability in the Lorenz system: A broken butterfly," *Int. J. Bifurcation and Chaos* **24**, 1450131–1–7.
- Lorenz, E. N. [1963] "Deterministic nonperiodic flow," *J. Atmosph. Sci.* **20**, 130–141.
- Moon, S., Seo, J. M., Han, B.-S., Park, J. & Baik, J.-J. [2019] "A physically extended Lorenz system," *Chaos* **29**, 063129.
- Munmuangsaen, B. & Srisuchinwong, B. [2018] "A hidden chaotic attractor in the classical Lorenz system," *Chaos Solit. Fract.* **107**, 61–66.
- Pal, S., Sahoo, B. & Poria, S. [2014] "Multistable behaviour of coupled Lorenz–Stenflo systems," *Phys. Scripta* **89**, 045202.
- Park, J., Lee, H., Jeon, Y.-L. & Baik, J.-J. [2015] "Periodicity of the Lorenz–Stenflo equations," *Phys. Scripta* **90**, 065201.
- Park, J., Han, B.-S., Lee, H., Jeon, Y.-L. & Baik, J.-J. [2016] "Stability and periodicity of high-order Lorenz–Stenflo equations," *Phys. Scripta* **91**, 065202.
- Pham, V.-T., Jafari, S., Volos, C., Wang, X. & Golpayegani, S. M. [2014] "Is that really hidden? The presence of complex fixed-points in chaotic flows with no equilibria," *Int. J. Bifurcation and Chaos* **24**, 1450146–1–6.
- Reyes, T. & Shen, B.-W. [2019] "A recurrence analysis of chaotic and non-chaotic solutions within a generalized nine-dimensional Lorenz model," *Chaos Solit. Fract.* **125**, 1–12.
- Roy, A., Roy, S. & Misra, A. P. [2019] "Dynamical properties of acoustic-gravity waves in the atmosphere," *J. Atmosph. Solar-Terrestrial Phys.* **186**, 78–81.
- Sahoo, B. [2013] "Numerical bifurcation and Hopf continuation of Lorenz–Stenflo system," *Phys. Scripta* **88**, 065011.
- Seydel, R. [1987] "New methods for calculating the stability of periodic solutions," *Comput. Math. Appl.* **14**, 505–510.
- Shen, B.-W. [2019] "On the predictability of 30-day global mesoscale simulations of African easterly waves during summer 2006: A view with the generalized Lorenz model," *Geosciences* **9**, 281.
- Sparrow, C. [1982] *The Lorenz Equations: Bifurcations, Chaos, and Strange Attractors* (Springer-Verlag, NY).
- Sprott, J. C. [2015] "New chaotic regimes in the Lorenz and Chen systems," *Int. J. Bifurcation and Chaos* **25**, 1550033–1–7.
- Stenflo, L. [1996] "Generalized Lorenz equations for acoustic-gravity waves in the atmosphere," *Phys. Scripta* **53**, 83–84.
- Stenflo, L. & Shukla, P. K. [2009] "Nonlinear acoustic-gravity waves," *J. Plasma Phys.* **75**, 841–847.
- Van Gorder, R. A. [2013] "Shil'nikov chaos in the 4D Lorenz–Stenflo system modeling the time evolution of nonlinear acoustic-gravity waves in a rotating atmosphere," *Nonlin. Dyn.* **72**, 837–851.
- Veronis, G. [1968] "Effect of a stabilizing gradient of solute on thermal convection," *J. Fluid Mech.* **34**, 315–336.
- Xavier, J. C. & Rech, P. C. [2010] "Regular and chaotic dynamics of the Lorenz–Stenflo system," *Int. J. Bifurcation and Chaos* **20**, 145–152.
- Yorke, J. A. & Yorke, E. D. [1979] "Metastable chaos: The transition to sustained chaotic behavior in the Lorenz model," *J. Statist. Phys.* **21**, 263–277.
- Yu, M. Y. [1999] "Some chaotic aspects of the Lorenz–Stenflo equations," *Phys. Scripta* **T82**, 10–11.